Radar penetrates only the youngest geological units on Mars

David E. Stillman[1] and Robert E. Grimm[1]

[1] Signals from the Shallow Radar were intended to penetrate hundreds of meters or more into Mars, but subsurface reflections are abundant only in known or inferred ice-rich units and young (middle to late Amazonian), apparently pristine, volcanic units. As volcanic units age, fewer subsurface reflections are detected. Also, no subsurface reflections are detected from any northern hemisphere units inferred to be altered by water. We suggest that the general lack of subsurface reflections on Mars is not likely an indication that the shallow interior is devoid of structure and stratigraphy but rather an indication that dielectric contrasts cannot be detected due to signal attenuation originating from scattering and/or absorption. We constrained the attenuation rate in regions with no subsurface reflections to 0.065–0.27 dB/m. This corresponds to scattering losses from meter-scale fractures and/or lithologic density variations of 0.27–1.03 g/cm^3. Alternatively, our laboratory measurements have shown that three monolayers of adsorbed water on 2.2–14 vol % smectite clays can completely absorb radar energy and would be equivalent to a global water layer just ~0.2–0.6 m thick. We suggest that the increased attenuation in volcanic units comes from an increase in fracture density. Attenuation in water-altered units may be due to the greater heterogeneity in sedimentary units and/or chemical alteration that has formed high-surface-area smectites capable of holding the necessary amount of adsorbed water. Overall, the lack of widespread, deep subsurface reflections is due to the more Earth-like radar properties of Mars, as compared to the Moon-like properties that were anticipated.

Citation: Stillman, D. E., and R. E. Grimm (2011), Radar penetrates only the youngest geological units on Mars, *J. Geophys. Res.*, *116*, E03001, doi:10.1029/2010JE003661.

1. Introduction

[2] A principal objective of the 20 MHz orbital surface-penetrating radar Shallow Radar (SHARAD) on board Mars Reconnaissance Orbiter was to detect echoes (reflections) from up to 1 km deep in the rocky Martian subsurface [*Seu et al.*, 2004]. In practice, however, reflections from such depths are evident only in ice-rich materials [e.g., *Seu et al.*, 2007b; *Holt et al.*, 2008; *Phillips et al.*, 2008; *Plaut et al.*, 2009a; *Putzig et al.*, 2009]. Indeed, over most of the surface of Mars, the only detected reflection is that of the planetary surface itself, and where reflections from the subsurface exist, they are rarely more than 100 m deep.

[3] Individual lava flows and sedimentary beds on Mars are typically meters to tens of meters thick, with some massive units up to hundreds of meters thick [*Beyer and McEwen*, 2005; *Keszthelyi et al.*, 2008; *Malin and Edgett*, 2000, 2003]. These sedimentary layers can be visually imaged in outcrop due to their differing erosion resistance (e.g., competent and noncompetent layers). The physical properties that change the competence of a layer often change the dielectric constant, which, on Earth, allows differences in erosion resistance to be detected via ground penetrating radar surveys [e.g., *Rother et al.*, 2007]. The general lack of subsurface reflections on Mars is therefore not likely an indication that the shallow interior is devoid of structure and stratigraphy, but rather that dielectric contrasts between geological units cannot be imaged due to attenuation of the radar signal. We investigated the origin of radar attenuation on Mars by qualitative association of radar reflectivity with surface geology and by quantitative assessment of absorption and scattering losses.

2. SHARAD Interpretation Methodology

[4] SHARAD transmits a chirped signal from 15 to 25 MHz and records the strength and delay time of reflected energy [*Seu et al.*, 2007a]. Pulse compression restores the signal to an approximate impulse response. The vertical (range) resolution is 15 m in free space; dividing by the square root of the real dielectric constant gives the vertical resolution in dielectric media. The spatial resolution perpendicular to the spacecraft ground track is 3–6 km, the diameter of the Fresnel zone. Doppler filtering improves the along-track resolution to 0.3–1 km.

[5] For this study, SHARAD Reduced Data Records through the 10th release (>1,000 radargrams) were indi-

[1]Department of Space Studies, Southwest Research Institute, Boulder, Colorado, USA.
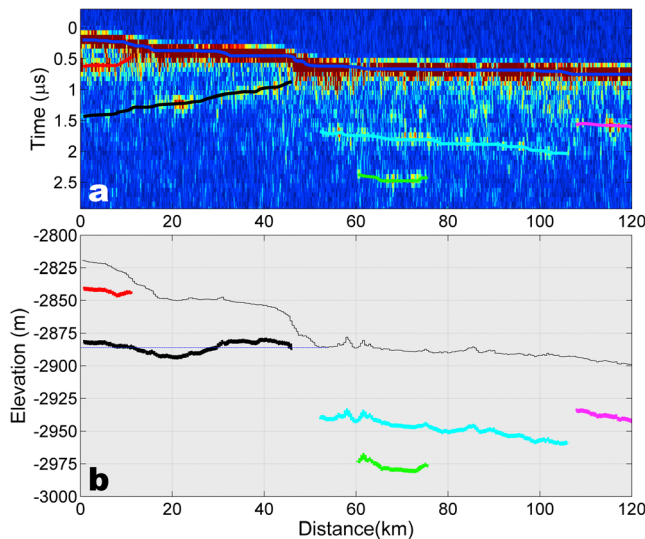
Figure 1. (a) Interpreted SHARAD track 0742703 radargram where low amplitude is blue and high amplitudes are red. The surface reflection (blue line) has been clipped to enhance the color contrast at later times. Our interpretations of subsurface reflections are overlaid on the radargram as colored lines. (b) Depth of reflections assuming $\varepsilon' = 8.8$, which restore the black reflector to assumed horizontality (thin blue line). The ground surface between SHARAD traverse of 18–50 km concurs with lava flow "ζ" from *Vaucher et al.* [2009].

vidually interpreted (Figure 1a). Subsurface reflections were picked on radargrams as amplitudes that are later than the surface reflection, are continuous, and could be ruled out as clutter (off-nadir reflections from topography). If a reflection was detected in an adjacent orbit track at nearly the same time delay, it is unlikely to be clutter. If there were no nearby SHARAD data, gridded MOLA topography was used to determine if there was any possible clutter-generating relief nearby. If there was, then we projected the reflection onto the planetary surface on both sides of the ground track to see if it aligned with any surface features [e.g., *Holt et al.*, 2008].

3. Near-Surface Dielectric Constant

[6] The velocity of the signal in the ground must be determined to convert reflection delay time into depth. The velocity v is inversely proportional to the square root of the real part of the relative dielectric constant ε': $v = c/\sqrt{\varepsilon'}$ where c is the speed of light in vacuum. Ice has $\varepsilon' = 3.15$ that is nearly independent of temperature (below the melting point) and ionic impurities at radar frequencies [*Matsuoka et al.*, 1997]. Most dry rocks at radar frequencies and Martian subsurface temperatures have ε' that is dominated by electronic polarization and hence bulk density ρ: $\varepsilon' = (1.93 \pm 0.17)^{\rho}$ [*Olhoeft and Strangway*, 1975]. As the density of basaltic rocks varies between ~2.1–3.3 g/cm^3 [*Johnson et al.*, 1984], we can constrain ε' to ~4–9 over the rocky units of Mars. Therefore, if ε' can be estimated, we can gain insight into the density of rocky units.

[7] We estimated ε' of two units in Elysium Planitia where the depth to the reflector can be assumed. In the Cerberus Fossae 3 unit (AEc$_3$ [*Tanaka et al.*, 2005]), the "ζ" lava flow [*Vaucher et al.*, 2009] has a distinct subsurface reflector. This flow sits ~25–35 m above the surrounding basaltic plains [*Tanaka et al.*, 2005; *Vaucher et al.*, 2009]. We inverted for the velocity, and thus ε', by using a nonlinear Levenberg-Marquardt least squares fit to minimize the difference between the elevation of the surrounding plains and the depth-corrected reflector (Figure 1b). A total of 39 SHARAD tracks were fit to yield $\varepsilon' = 8.8 \pm 1.0$, a value consistent with a basaltic lava flow of $\rho = 3.3 \pm 0.6$ as interpreted by *Tanaka et al.* [2005] and *Vaucher et al.* [2009].

[8] Our second example is the Medusae Fossae unit (AAm). *Watters et al.* [2007] derived $\varepsilon' = 2.9 \pm 0.4$ using MARSIS (a 1.3–5.5 MHz orbital radar), assuming the reflection came from the base of AAm, which corresponds to the elevation of the surrounding plains. Using SHARAD, *Carter et al.* [2009] reported $\varepsilon' \sim 3$ assuming the reflector came from a layer that outcrops as a talus slope to the north and forms the valley floor to the south of North Hill. However, this valley floor is not composed of unit AEc$_3$ (the surrounding plains), but rather an exposed older subunit of AAm [*Mandt et al.*, 2009]. We assumed this exposed older subunit was horizontal and used it as our datum. By fitting seven SHARAD tracks over North Hill, we obtained $\varepsilon' = 3.9 \pm 0.6$ using the same method as discussed above. The low ε' and attenuation of North Hill is consistent with either an ice-rich composition [*Watters et al.*, 2007] or a dry ignimbrite [*Tanaka et al.*, 2005; *Mandt et al.*, 2009; *Zimbelman and Griffin*, 2010].

[9] The older exposed subunit of the AAm most likely continues under the thicker hill to the south of North Hill. MARSIS data [*Watters et al.*, 2007] detects the older exposed subunit of the AAm continues under the thicker hill to the south of North Hill. However, it is not detected in any of the SHARAD tracks. This contradiction indicates that AAm is attenuating radar energy at SHARAD frequencies.

4. SHARAD Correlation to Geologic Units

[10] SHARAD tracks and subsurface reflections were overlaid on a geologic map of the northern plains [*Tanaka et al.*, 2005] (Figure 2). Analysis was restricted to the northern plains because the stratigraphy is better defined and surface scattering (clutter) is less than for the southern cratered highlands. In fact, all mapped units dominated by crater materials were discarded. We found that there is a striking correlation in the remaining 38 unit types between the presence of subsurface reflections and specific surface geologic units (Figure 2). Note that all units were not sampled at an equivalent density.

[11] The results were cross-classified according to the radar response and geological nature of surface units. "Abundant reflections," "occasional reflections," and "no reflections" comprised those geologic units in which >50%, <50%, and none of the radargrams in that unit showed subsurface reflections, respectively. Geological unit descriptions [*Tanaka et al.*, 2005] were sorted into three categories: "ice rich," "pristine volcanic," and "water altered" (Table 1). The
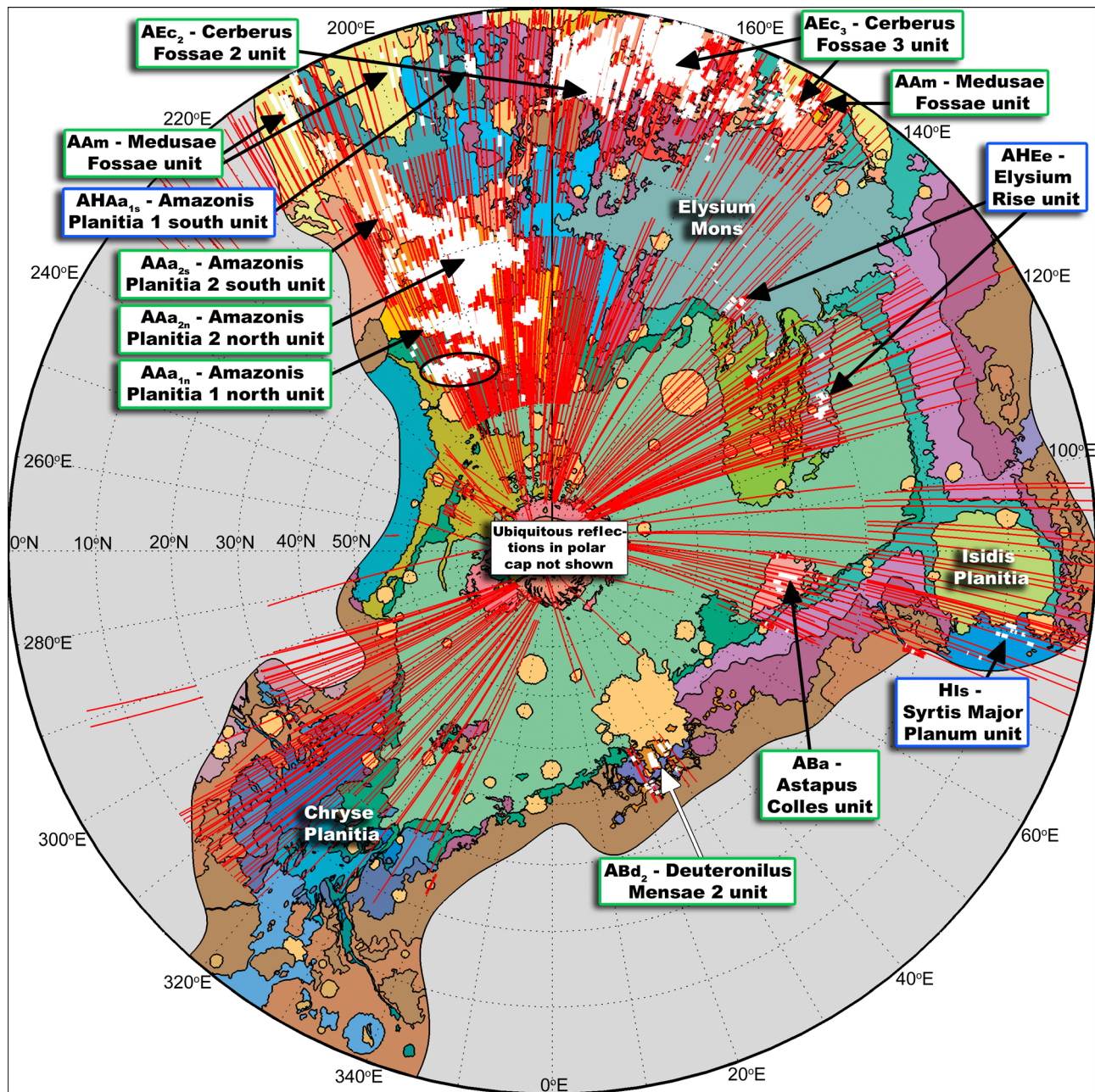
Figure 2. Geologic map of the northern plains of Mars [*Tanaka et al.*, 2005] showing SHARAD tracks (red) and subsurface reflections (white). All nonpolar units with reflections are labeled with a green box color indicating abundant reflections and blue indicating occasional reflections in the unit. Reflection occurrence is well correlated with unit definitions except in the oval to the north of AAa_{1n}, which is inferred to be ice rich (see Appendix A).

first group comprises the northern polar cap as well as units whose morphology suggests the presence of ice [*Holt et al.*, 2008; *Plaut et al.*, 2009a]. The second group consists of lava flows and volcaniclastics that have no descriptions of significant aqueous alteration. The third group encompasses all units that were interpreted to have been formed by, or been modified by, water in fluvial, lacustrine, or periglacial processes. The processes in this category include groundwater sapping and reworking of sediments, fluvial erosion, sedi-

mentary deposition, mud volcanism, and magma/volatile interactions.

[12] We found that reflection abundance correlates strongly with the age of geological units (Figure 3). Abundant reflections are restricted to the Amazonian. Indeed, 10 of the 11 mapped units with abundant reflections may be as young as late Amazonian. Occasional reflections are found in units with greater ages, from the early Hesperian to the early Amazonian. Units with no reflections span Noachian to middle Amazonian ages.

Table 1. Categorization of *Tanaka et al.*'s [2005] Descriptions Into Three Classifications: Ice Rich, Pristine Volcanic, and Water Altered[a]

Age	Unit	Description	Classification
Late Amazonian	ABb_2	polar cap	ice rich
	ABb_1	polar cap	ice rich
	ABo	polar cap	ice rich
	ABa	volatile-rich flow or mantle	ice rich
	ABd_2	ice-lubricated deposits from mass wasting	ice rich
	AEc_3	voluminous lava flows and perhaps minor fluvial deposits	pristine volcanic
	AEc_2	lava flows	pristine volcanic
	AAm	volcanic ash deposits	pristine volcanic
	AAa_{2n}	lava flows and perhaps fluvial sediments	pristine volcanic
	AAa_{2s}	voluminous lava flows	pristine volcanic
Middle Amazonian	ATl	shield lavas moved by landsliding/gravity spreading	pristine volcanic
	AAa_{1n}	lava and perhaps volcaniclastic flows	pristine volcanic
	AEc_1	possibly periglacial and groundwater processes	water altered
	ABs	mud volcanism	water altered
Early Amazonian	AEt_b	fluvial deposits and debris flows	water altered
	AEt_a	massive volcaniclastic flows from magma/volatile interactions; subsequent modification from volatile escape	water altered
	ABV_m	reworked sediments, perhaps by groundwater	water altered
	ABV_i	sediments reworked by periglacial processes	water altered
	AIi	sedimentary rapidly emplaced by water	water altered
	$AHEe$	lava flows and possibly other volcanics	pristine volcanic
	$AHAa_{1s}$	lava flows and perhaps debris flows	pristine volcanic
Late Hesperian	HAa	mass wasting of volatile-rich, near-surface rocks	water altered
	HCs	blocks and debris disrupted and transported by volatile-rich material	water altered
	HCa	indurated cap layer (but with olivine)	water altered
	HCc_4	debris flows and/or rapidly emplaced fluvial sediments	water altered
	HCc_3	fluvial deposits	water altered
	HCc_2	fluvial deposits and debris flows	water altered
	HBu_2	redeposition of earlier materials	water altered
	HTa	basaltic flows with some ash flows/lahars	pristine volcanic
	HIs	basaltic lava flows	pristine volcanic
Early Hesperian	$HNTl$	basaltic sheet flows	pristine volcanic
	HIa	lava or debris flows	pristine volcanic
	HNn	mass wasting	water altered
	$HNCc_1$	mass wasting and fluvial erosion	water altered
	HBu_1	clastic deposits	water altered
	HBd_1	ice-rich debris mass wasting	water altered
Noachian	Nl	mixture of volcanics, sedimentary, impact melt, and ejecta	water altered
	Nn	mixture of volcanics and sedimentary material	water altered

[a]Units AEc_3 and AEc_2 have had their underlying morphology altered by water [*Jaeger et al.*, 2007] and show signs of surface volcanic-water interactions (rootless cones) [*Lanagan et al.*, 2001; *Fagents et al.*, 2002]. In regions of rootless cones there are no SHARAD reflections. However, the majority of these units contain no rootless cones. These regions are apparently pristine and SHARAD reflections are abundant. Therefore, we consider these units as pristine volcanics to highlight what is occurring in the majority of the units.

[13] Reflection abundance also correlates strongly with the type of geological unit (Figure 3). The ice-rich polar cap units have numerous internal and/or basal reflections and were natural targets for extensive analysis by previous workers [e.g., *Phillips et al.*, 2008; *Putzig et al.*, 2009]. Internal absorption and scattering must be small, in analogy with terrestrial polar ice. The radar transparency of Deuteronilus Mensae 2 unit (ABd_2) [*Plaut et al.*, 2009a] supports the idea that these midlatitude, ice-lubricated, debris flows still contain volatiles, preserved from an earlier climate epoch. A similar response from Astapus Colles unit (ABa), interpreted as a volatile-rich flow or mantle unit, leads us to similarly suggest that this midlatitude unit is ice rich.

[14] Pristine volcanics span the full range of reflection occurrence, with the youngest units having abundant reflections, older units having occasional reflections, and the oldest units having no reflections (Figure 3). The only exception is the middle Amazonian Lycus Sulci unit (ATl) that shows no subsurface reflections. However, the amount of energy that can penetrate into this unit may be limited due to scattering from its very rough surface. Furthermore, this formation appears to have been moved by landsliding or gravity spreading [*Tanaka et al.*, 2005], which may have intensely fractured its interior, causing further scattering of radar energy. The only reflections detected in water-altered units (oval in Figure 2) occur in a small part of the Vastitas Borealis marginal unit (ABv_m) and Scandia region unit (ABs). This is also the only location where a reflector crosses a geologic boundary. Therefore, we infer that these reflections are due to ice-rich material superimposed on the regional geology [*Plaut et al.*, 2009b; *Byrne et al.*, 2009] (see Appendix A). The lack of reflections detected in the majority of water-altered units is the focus of the remainder of this paper.

5. Attenuation Rates of Rocky Mars

[15] Attenuation is defined here as the part of the energy loss in the radar signal that is not explained by transmission
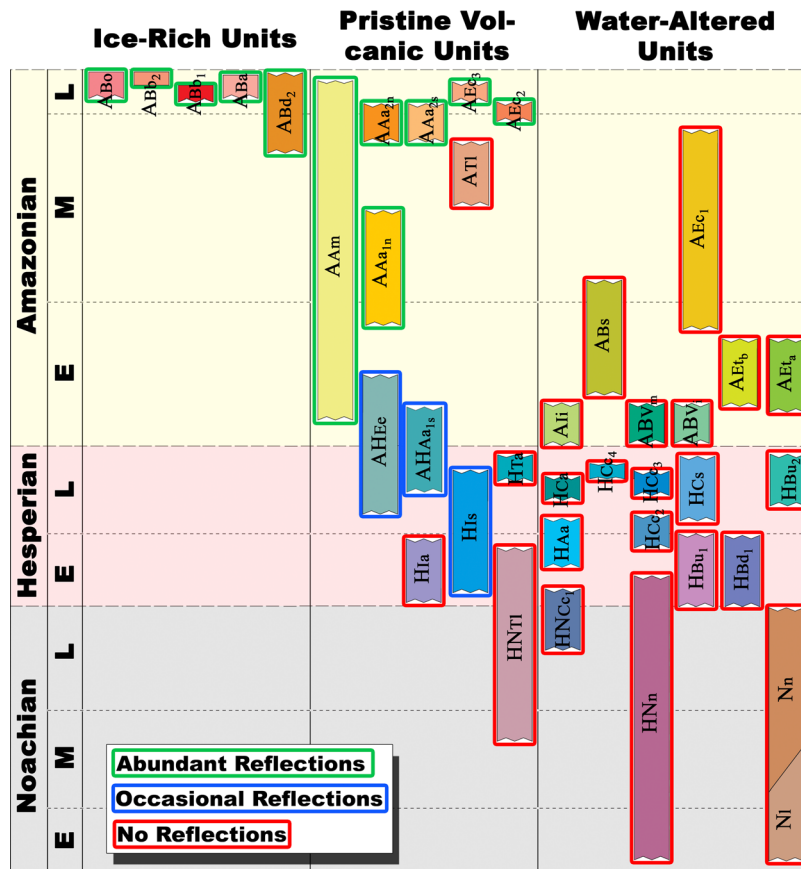
Figure 3. Unit ages [*Tanaka et al.*, 2005] with unit colors corresponding to Figure 2. The outline color (green, blue, and red) of the units indicates the occurrence of reflections (see section 4 for definitions). Almost all of the youngest volcanic units have abundant reflections.

and reflection in a dielectric medium [e.g., *Ulaby et al.*, 1981]. The attenuation rate η (dB/m) for a layer over a half-space at normal incidence is:

$$\eta = \frac{\Delta S - \Delta S_R}{2d_1} \tag{1}$$

$$\Delta S = 20 \log(A_r/A_0) \tag{2}$$

$$\Delta S_R = 2T_{01} + R_{12} - R_{01}. \tag{3}$$

$$R_{xy} = 10 \log \left(\left| \frac{\sqrt{\varepsilon_x} - \sqrt{\varepsilon_y}}{\sqrt{\varepsilon_x} + \sqrt{\varepsilon_y}} \right|^2 \right) \tag{4}$$

$$T_{xy} = 1 - R_{xy} = 10 \log \left(\frac{4\sqrt{\varepsilon_1'}\sqrt{\varepsilon_2'}}{\left(\sqrt{\varepsilon_1'} + \sqrt{\varepsilon_2'}\right)^2} \right) \tag{5}$$

where ΔS is the ratio of the power of the weakest detected subsurface reflector to the power of the surface reflection, A_r is the amplitude of the weakest detected subsurface reflection, A_0 is the amplitude of the surface reflection, ΔS_R is the ratio of the subsurface reflected power to the surface reflected power assuming no losses, T is the power trans-

mission coefficient, R is the power reflection coefficient, x and y subscripts denote adjacent layers (0, 1, 2 denote the overlying vacuum, the layer, and the half-space, respectively), and d_1 is the thickness of layer 1. From regions of strong reflectivity, we found that $\Delta S = -19$ dB, which is comparable to the $\Delta S = -16$ dB interpreted by *Campbell et al.* [2008]. By computing an average trace for multiple SHARAD RDRs, we determined that the noise floor of the data was -24 ± 5 dB when compared to the surface reflection.

[16] Next, we constructed Table 2 to demonstrate that a dielectric contrast $\Delta\varepsilon' \geq 0.7–2.3$ between two layers is needed to create a detectable reflection ($\geq\Delta S$) in the absence of subsurface attenuation. If constructive interference occurs, $\Delta\varepsilon' < 1$ can create detectable reflections, as could be the case in the Martian north polar layered deposits [*Putzig et al.*, 2009]. It is likely that $\Delta\varepsilon' > 1$ occurs between competent and noncompetent erosional layers that have been visually imaged [*Malin and Edgett*, 2000; *Beyer and McEwen*, 2005]. Therefore, significant subsurface attenuation must be taking place.

[17] We specified a range of possible depths and ε' for likely subsurface interfaces to estimate attenuation rates with units lacking subsurface reflections. The maximum attenuation rate is determined by the minimum depth to which SHARAD can resolve a reflection, which in turn is determined by the radar bandwidth, noise floor, digitization rate

Table 2. ΔS_R in dB as a Function of ε' for Layer 1 and 2 (Reflector)[a]

Layer 1 ε'_1	Reflector ε'_2										
	3	3.15	4	5	6	7	8	9	12	15	20
3	nr	**−27.5**	−12.1	−7.1	−4.5	−2.8	−1.6	−0.6	*1.2*	*2.4*	*3.7*
3.15	**−27.9**	nr	−14.1	−8.4	−5.6	−3.7	−2.4	−1.4	*0.5*	*1.8*	*3.1*
4	−14.4	−16.0	nr	−16.6	−11.4	−8.6	−6.8	−5.5	−2.9	−1.4	*0.2*
5	−10.9	−11.8	−18.1	nr	**−19.8**	−14.5	−11.6	−9.7	−6.3	−4.4	−2.6
6	−9.5	−10.1	−14.1	**−21.0**	nr	**−22.4**	−17.0	−14.1	−9.5	−7.1	−4.8
7	−8.7	−9.2	−12.2	−16.6	**−23.4**	nr	**−24.6**	**−19.1**	−12.5	−9.6	−6.9
8	−8.2	−8.6	−11.1	−14.5	−18.7	**−25.4**	nr	**−26.5**	−15.7	−12.0	−8.8
9	−7.9	−8.3	−10.5	−13.2	−16.4	−20.5	**−27.1**	nr	**−19.4**	−14.4	−10.6
12	−7.5	−7.8	−9.4	−11.3	−13.3	−15.5	−17.9	**−20.9**	nr	**−23.1**	−15.9
15	−7.5	−7.7	−9.0	−10.6	−12.1	−13.6	−15.3	−17.0	**−24.2**	nr	**−22.0**
20	−7.6	−7.8	−8.9	−10.1	−11.2	−12.3	−13.5	−14.6	−18.4	**−23.4**	nr

[a]Note that when there is no contrast between the two layers, there is no reflection (nr). Reflections that would not be interpretable in SHARAD are shown in bold as the $\Delta S_R < \Delta S$. Therefore, $\Delta \varepsilon' = 0.7–2.3$ is needed to detect a subsurface reflection with no subsurface attenuation. Note that for $\varepsilon'_2 \geq 12$ and $\varepsilon'_1 \leq 4$, the ΔS_R are positive (italics). This is due to the small R_{01} and large R_{12}. Dielectric constants greater than 12 would indicate wet or highly altered rocks.

(0.075 μs), and the window function (nominally Hanning). We used a one-dimensional full-waveform model [*Grimm*, 2002; *Nunes and Phillips*, 2006] to determine a minimum resolvable two-way travel time (Figure 4). To compute the maximum attenuation rate and minimum resolvable two-way travel time, we assumed the largest dielectric contrast typical of dry rocks. The minimum resolvable two-way travel time was found to be 0.33 μs, which corresponds to $d_1 = 24.75$ m at $\varepsilon'_1 = 4$ and $\varepsilon'_2 = 9$, or $d_1 = 16.5$ m at $\varepsilon'_1 = 9$ and $\varepsilon'_2 = 4$. The maximum attenuation rate is then ~0.27 dB/m (Table 3). A more representative or nominal attenuation rate of ~0.065 dB/m was determined using a two-way reflection time of 0.75 μs and $\varepsilon'_1 = 5$ or 8 and $\varepsilon'_2 = 8$ or 5 (Table 3). The two-way reflection time was picked so that the reflector would be 40–50 m deep, which was the approximate layer thickness of the majority of units with abundant reflections.

[18] *Campbell et al.* [2008] computed loss tangents and ΔS_R by fitting the reflection strength to the two-way travel time for the Amazonis Planitia 2 north unit (AAa_{2n}). Their ΔS_R have an average value of −7.4 dB (i.e., the intercept of their attenuation function fits), indicating that this reflection cannot be caused by a higher ε' to a lower ε' interface (i.e., $\varepsilon'_1 = 9$ and $\varepsilon'_2 = 4$ gives ΔS_R of −10.5 dB; thus in order for ΔS_R to be ≤ -7.4 dB, then ε'_1 must be ≤ 4.4 and $\varepsilon'_2 = 9$). We combined *Campbell et al.* [2008] loss tangents with ε' ranging from 4 to 4.4 to yield an attenuation rate of 0.018–0.046 dB/m. The upper bound of this attenuation rate is slightly lower than the lower bound of the assumed nominal attenuation rate of 0.057 dB/m, thus indicating the nominal rate is greater than the attenuation rate in a unit with reflectors.

[19] We were unable to extend the *Campbell et al.* [2008] technique to the AEc_3 and AAm units because of the large scatter in reflected energy. Therefore, we measured the power and delay time of the deepest reflection in both units (SHARAD track 657001 and 186301 for AEc_3 and AAm, respectively). We computed ΔS_R assuming the maximum reflection coefficient of dry rocks and ε'_1 derived in section 3. The attenuation rate was computed by taking the ratio (difference in dB) of the average power of the reflection to ΔS_R and then dividing by two times the depth of the reflection. This yielded attenuation rates of ≤ 0.031 and ≤ 0.014 dB/m for AEc_3 and AAm, respectively. These attenuation rates are upper limits because their reflection coefficients assumed the maximum dielectric contrast of dry rocks. The attenuation rates in geological units lacking subsurface reflections are higher than those in which reflections are evident (Table 4).

6. Mechanisms of Martian Attenuation

[20] Units with abundant reflections have similar attenuation rates to the Moon, ~0.008–0.074 dB/m [*Carrier et al.*, 1991], whereas our calculated maximum attenuation rate exceeds this range. Lunar attenuation is primarily a function of ilmenite content [*Schaber et al.*, 1975; *Carrier et al.*, 1991]. Attenuation rates for Mars are in the lower end of those
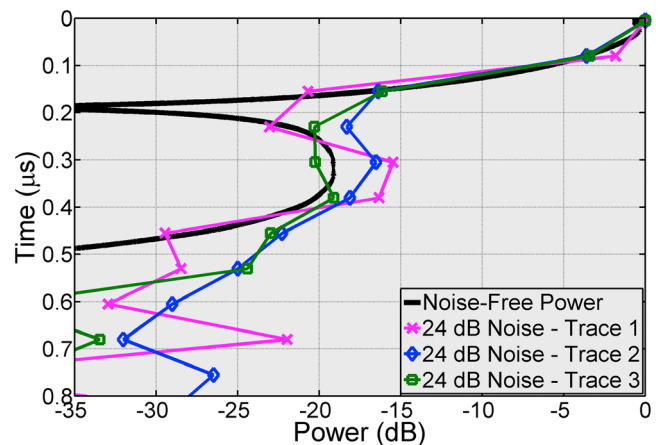
Figure 4. Modeled radar return of the shallowest (0.33 μs) interpretable reflection assuming the largest dry rock reflection coefficient. The top layer has an attenuation rate of 0.27 dB/m with $\varepsilon'_1 = 4$, $\varepsilon''_1 = 0.292$, and depth of 24.75 m, while the bottom layer has $\varepsilon'_2 = 9$. The noise-free power shows that shallower reflections could be identified with a smaller data time interval and no noise. Three synthetic SHARAD traces with symbols at the SHARAD time interval and with noise added demonstrate that 0.33 μs is the shallowest interpretable reflection depth, as at least one data point must be lower than the strength of the reflection, in order to confidently interpret a reflection.

Table 3. Derivation of Maximum and Nominal Attenuation Rates

	Maximum Attenuation Rate		Nominal Attenuation Rate	
	High ε_1' Over Low ε_2'	Low ε_1' Over High ε_2'	High ε_1' Over Low ε_2'	Low ε_1' Over High ε_2'
Layer ε_1'	9	4	5	8
Layer 1 thickness (μs)	0.33	0.33	0.75	0.75
Layer 1 thickness (m)	16.5	24.8	50.3	39.8
Half-space ε_2'	4	9	8	5
ΔS_R (dB)	−10.5	−5.5	−11.6	−14.5
Attenuation[a] (dB)	−8.5	−13.5	−7.4	−4.5
Attenuation rate (dB/m)	0.259	0.274	0.073	0.057

[a]Numerator in equation (1).

measured for terrestrial rocks and soils, ~0.01–100 dB/m [*Annan*, 2003]. Water is by far the greatest contributor to high absorption on Earth, through electrolytic conduction and dielectric relaxation. A scattering attenuation rate of ~0.5 dB/m at 25 MHz in the Bishop (CA) tuff [*Grimm et al.*, 2006] may be typical of fractured rocks. We calculated limits to scattering heterogeneity and absorption constituents that could cause the inferred attenuation rates on Mars.

6.1. Scattering

[21] We used the classical, Born approximation [*Aki and Chouet*, 1975] to compute the losses due to single scattering. This allows us to constrain the range of scatterer sizes and dielectric contrasts needed to produce the inferred attenuation rates. A random heterogeneous medium with spatially varying velocity can be characterized by an autocorrelation function [*Aki and Chouet*, 1975]:

$$N(r) = \frac{\left\langle \frac{\Delta V}{V}(r') \frac{\Delta V}{V}(r' + r) \right\rangle}{\left\langle \frac{\Delta V^2}{V} \right\rangle} \quad (6)$$

where $\Delta V/V$ is the random fractional velocity perturbation and r is distance. We then treated $\Delta V/V$ as either an exponential autocorrelation function (EAF), $N_{EAF}(r) = e^{-r/a}$, or a Gaussian autocorrelation function (GAF), $N_{GAF}(r) = e^{-r^2/a^2}$. The attenuation rates are [*Aki and Chouet*, 1975]:

$$\eta_{EAF} = \frac{34.744 k^4 a^3 \left(\frac{\Delta V}{V} \right)^2}{(1 + 2k^2 a^2)^2} \quad (7)$$

$$\eta_{GAF} = 4.343 \sqrt{\pi} k^4 a^3 \left(\frac{\Delta V}{V} \right)^2 e^{-0.5 k^2 a^2} \quad (8)$$

where η_{EAF} is the attenuation rate for the EAF, η_{GAF} is the attenuation rate for the GAF, a is the correlation length or the physical length scale of the heterogeneous scatterer, and k is the wave number [*Aki and Chouet*, 1975]. Both of these functions reproduce Rayleigh scattering (attenuation rate increasing as frequency to the fourth power) for $ka \ll 1$, but differ at high frequency, $ka \gg 1$, as the extended shape

function of the exponential autocorrelation function converges to the geometric optics limit.

[22] The Born models show that scattering attenuation rates require the minimum velocity variation at heterogeneity scales of 1–2 m (Figure 5). The velocity variation can then be converted to determine ε' and the density contrast of the scatterers. To produce the maximum attenuation rate (0.27 dB/m), peak density contrasts up to 0.65–1.03 g/cm^3 are required; such contrasts are consistent with terrestrial lithologic heterogeneity and/or fractures filled with unconsolidated material. To produce the nominal attenuation rate, peak density contrasts of just 0.27–0.42 g/cm^3 are required. Another possibility is that strong lateral variations at scales of hundreds of meters, (i.e., much larger than a wavelength in the ground, but smaller than the Fresnel zone) could make the returned energy incoherent. By contrast, the radar-transparent units of AAm and AEc$_3$ must be coherent within
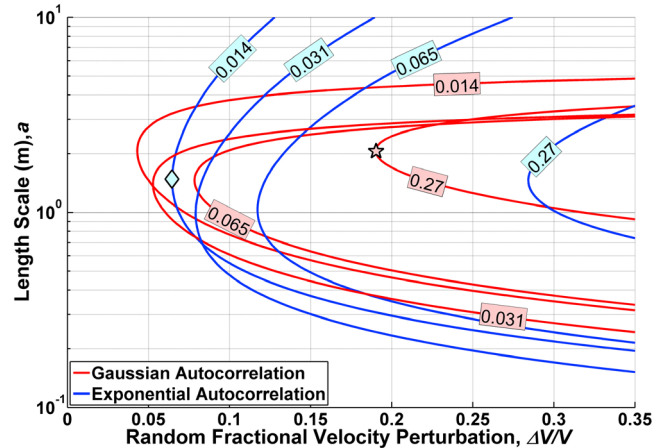
Figure 5. Born scattering (dB/m) at 20 MHz for two auto-correlation functions. The maximum and AAm attenuation rates (0.27 and 0.014 dB/m, respectively) assume a medium $\varepsilon_1' = 4$, while the nominal and AEc$_3$ attenuation rates (0.065 and 0.031 dB/m, respectively) assume a medium $\varepsilon_1' = 8$ and 8.8, respectively. For a Gaussian autocorrelation function, 2 m heterogeneity with ~19% velocity variations (scatterers with $\varepsilon' = 6.1$) yields maximum attenuation rate in radar-opaque Mars units, ~0.27 dB/m (star). The same loss can be achieved away from the optimum scatterer size with larger velocity contrast. For an exponential autocorrelation function, velocity contrasts in radar transparent units such as AAm are restricted to ~7% velocity variations at the 1.4 m scale (diamond).

Table 4. Comparison of Attenuation Rates

Maximum	Nominal	AAa$_{2n}$[a]	AEc$_3$	AAm
0.259–0.274	0.057–0.073	0.018–0.046	<0.031	<0.014

[a]From *Campbell et al.* [2008] assuming ε' values of 4–4.4.
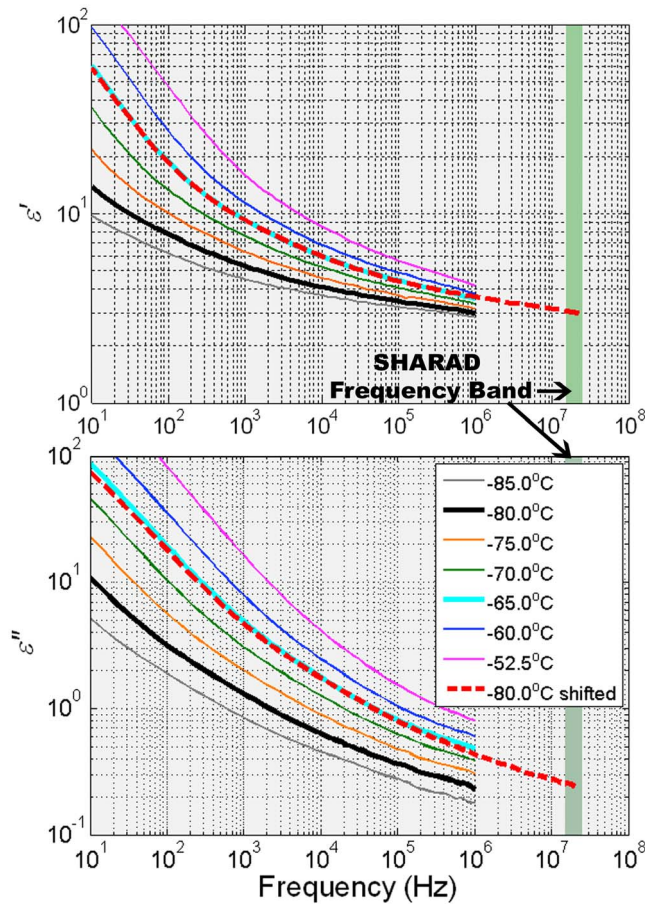
Figure 6. Our laboratory measurements of the low-frequency dispersion due to three monolayers of 1 M CaCl$_2$ aqueous solution on sand mixed with 9.67 vol % STx-1. Because the relaxation frequency follows a simple Arrhenius activation energy, we can extrapolate (top) ε' and (bottom) ε'' to SHARAD frequency simply by laterally shifting cold temperature data ($-80°C$) to the desired temperature ($-65°C$).

geological units on a scale of kilometers and would have maximum density contrasts <0.20 and <0.23 g/cm^3 (Figure 5), respectively, at the same 1–2 m length scales.

6.2. Absorption

[23] Alternatively, the radar attenuation can also be explained by energy absorption. The absorption of cold and dry silicate minerals is much too small [*Gueguen and Palciauckas*, 1994]. Even an ilmenite-rich lunar mare of 31.9 wt % (TiO$_2$ + FeO) yields an attenuation rate of only ~0.074 dB/m [*Carrier et al.*, 1991]. On Mars, ilmenite has not been found at high concentrations with the regolith only containing ~1 wt TiO$_2$ [*Rieder et al.*, 1997, 2004]. However, the presence of adsorbed water on any mineral will drastically increase electrical loss [*McCafferty and Zettlemoyer*, 1971; *Olhoeft et al.*, 1975]. This occurs not by conduction, but through dielectric relaxations in and along the water layer [*Sjöström et al.*, 2008; *Stillman et al.*, 2010]. One to three monolayers of H$_2$O can be held at the humidity of Mars' surface, so a large surface area is necessary to retain substantial quantities of adsorbed water. Phyllosilicates,

particularly smectite clays, can readily provide such surface area.

[24] To test this hypothesis, we measured the complex dielectric constant $\varepsilon' - i\varepsilon''$ (where $i = \sqrt{-1}$ and ε'' is the imaginary part of the relative dielectric constant) as a function of temperature ($-90°C$ to $+25°C$), frequency (1 mHz to 10 MHz), smectite volume concentration (2.3%–32%), number of H$_2$O monolayers (1–7), salt type (CaCl$_2$, NaCl, MgSO$_4$), and salinity (0.01–3.5 M and no salt). See *Stillman et al.* [2010] for additional measurement details. The complex dielectric constant determines the attenuation rate η_ε at 20 MHz as: $\eta_\varepsilon = 1.82\sqrt{\varepsilon'}\varepsilon''/\varepsilon'$ (dB/m) [*Grimm et al.*, 2006]. We assumed an average Martian subsurface temperature of $-65°C$, as η_ε increases with temperature due to the temperature dependence of the complex dielectric constant.

[25] Our apparatus does not allow us to make measurements at the center frequency of SHARAD. However, the coldest measurements taken at $-90°C$ or $-85°C$ showed no indication of dielectric relaxations at higher frequencies (>1 MHz), which would have been detected first in an upslope in ε'' and then a decrease in ε' (Figure 6). Since no phase changes occur between $-65°C$ and $-80°C$, the only difference in the dielectric relaxation between data at these two temperatures is the temperature dependence in the relaxation frequency [e.g., *Kauzmann*, 1942] (Figure 6). This causes the dielectric relaxation at colder temperatures to shift to lower frequencies. Therefore, the $-80°C$ data can be shifted to higher frequency so that the low-frequency data matches the $-65°C$ and the high-frequency data extends into SHARAD frequencies (Figure 6).

[26] We used a calcium montmorillonite, STx-1 [*Costanzo*, 2001], with a H$_2$O specific surface area of 217 m^2/g [*Jänchen et al.*, 2009]. This smectite was mixed with fine-grained sand (specific surface area of 0.5 m^2/g) so that we could vary the bulk specific surface area of the sample. Before measuring, the sand-smectite mixture was dried in thermal vacuum at 115°C and 25 inches of Hg for at least a day. Next, small amounts of deionized water or salt solutions were added to the sample to obtain the correct number of H$_2$O monolayers. Adsorbed water (1–3 monolayers) creates a broadband temperature-dependent low-frequency dispersion [*Shahidi et al.*, 1975; *Stillman et al.*, 2010] that can attenuate radar energy. The strength of this dispersion increases with the number of monolayers from one to three, and with increased surface area. We found that 14 vol % smectite with three monolayers matched the 0.27 dB/m upper limit SHARAD attenuation rate, whereas only 3.6 vol % was required to produce the nominal attenuation rate of 0.065 dB/m (Figure 7). Our measurements show that <1 M Cl$^-$ salt has no effect on the dielectric relaxation, whereas the attenuation increases at concentrations ≥1 M Cl$^-$. Therefore, if the three water monolayers consisted of ≥1 M Cl$^-$, 9.5 vol % smectite yields the maximum attenuation rate, whereas only 2.2 vol % was required to produce the nominal attenuation rate. There was no affect on radar absorption when more than three monolayers of H$_2$O were present (Figure 7), since any additional monolayers are not adsorbed and form ice [*Anderson and Tice*, 1973; *Asay and Kim*, 2005; *Stillman et al.*, 2010].

[27] Using these results, a Martian global equivalent layer of adsorbed water was calculated. Three monolayers of H$_2$O
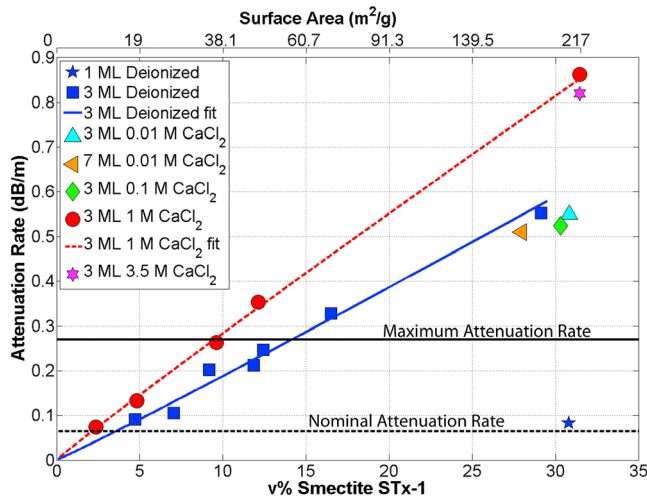
Figure 7. Absorption of SHARAD energy at −65°C with 1–7 monolayers (ML of H_2O) with differing amounts of $CaCl_2$. $CaCl_2$ concentrations of >1 M with three ML produce a ~33% increase in the attenuation rate. As the number of ML is increased to three, the attenuation rate also increases. However, at >3 ML the water is no longer adsorbed and turns to ice, thus leaving the attenuation rate unchanged (orange triangle).

on 2.2–14 vol % STx-1 are equal to 0.22–1.34 wt % adsorbed water. We found that abundant radar penetration only occurs in ~3% of the surface area of Mars: the polar caps, lobate debris aprons, and the young pristine volcanic units in the northern hemisphere. We then assumed the remaining area contains three monolayers of adsorbed water on 2.2 or 14 vol % high-surface-area smectite. This adsorbed water is equivalent to a global layer of only 0.59–0.62 and 0.15–0.22 m for the maximum and nominal attenuation rate, respectively. This water volume is nearly 2 orders of magnitude smaller than the global equivalent layer of 11 m in just the south polar layered deposits [*Plaut et al.*, 2007].

7. Discussion

[28] Phyllosilicates and adsorbed water have been detected on Mars in quantities comparable to or greater than those called for here. Phyllosilicate-like minerals at 5–31 vol % were inferred globally in midinfrared spectroscopy [*Michalski et al.*, 2006], although near-infrared (NIR) spectroscopy has only detected phyllosilicates in specific locations [e.g., *Bibring et al.*, 2006; *Milliken et al.*, 2007]. However, NIR spectroscopy has mapped adsorbed water globally with a concentration of ~2–5 wt % H_2O in the top millimeter from 0°N to 45°N latitude [*Milliken et al.*, 2007]. Furthermore, neutron spectroscopy (NS) indicates that the top meter of the Martian low-latitude (±45°) subsurface contains hydrogen at an amount equivalent to 2–10 wt % H_2O [*Feldman et al.*, 2004]. This H could be in the form of adsorbed water and/or phyllosilicates. Two of the areas of lowest H concentrations in the NS data are in Elysium and Amazonis Planitia, where radar penetration through rock is greatest. However, this correlation is imperfect elsewhere.

[29] The direct correlation of water-altered units and high radar attenuation can then be explained in two ways. First, the fluvial, lacustrine, or periglacial processes cited for geomorphological change [*Tanaka et al.*, 2005] could aqueously alter source materials to form high-surface-area minerals such as smectites or palagonites. Although almost all of the water was ultimately lost from these units, small quantities would have been retained in adsorption. Auxiliary salts were deposited when the water evaporated. This model implies that smectites are ubiquitous on Mars to depths of at least tens of meters. This hypothesis is strongly supported by the H abundance in the low-latitude NS data, but requires a threshold of several percent for NIR detection of smectites.

[30] Alternatively, radar loss in the water-altered units could be due to the high degree of heterogeneity introduced at the wavelength scale, or over the Fresnel zone, by geomorphological modification. In both models, the young, pristine volcanics must form with homogeneous interiors at these scales, and the older volcanics become progressively fractured and hence better radar scatterers. This progressive fracturing could be due to impact cratering and/or global thermal contraction [*Solomon et al.*, 1991].

[31] Scattering and adsorbed water probably both contribute to attenuating SHARAD radar energy on Mars. If all the attenuation is due to absorption, the Martian rates are between those of the Earth and the Moon. The lower absorption compared to Earth is dominated by the lack of free, liquid water, and supplemented by reduced fracturing and deformation on a tectonically more quiescent planet. The increased absorption compared to dry silicates is most easily explained by adsorbed water bound to small quantities of high-surface-area minerals produced during previous epochs of aqueous alteration on Mars. This comparison also suggests that the adsorbed water recently discovered on the Moon [*Clark*, 2009; *Pieters et al.*, 2009; *Sunshine et al.*, 2009] should not generate radar loss because there has not been any surface area–increasing mineralogical alteration and because adsorbed water in vacuum will average less than one monolayer.

8. Conclusion

[32] Subsurface radar transparency to depths of hundreds of meters or more is rare in rocky units at SHARAD and MARSIS frequencies on Mars. The premission overestimation of ground penetration was caused by optimistic assumptions about the scattering and electrical properties of the subsurface. The electrical properties of the subsurface of Mars may not be analogous to the Moon due to water alteration (i.e., smectites) and the increased attenuation is due to water adsorption. To better constrain and determine the relative contribution of absorption and scattering to attenuation, a broadband multifrequency ground penetrating radar instrument is necessary [e.g., *Grimm et al.*, 2006].

[33] In water-altered and old volcanic units, future radar systems must overcome hundreds of decibels in attenuation to probe the originally desired kilometer depths. Therefore other geophysical techniques must be used to search for groundwater, such as active seismic Q [e.g., *Tittmann*, 1979; *Olhoeft*, 2003], magnetotellurics [e.g., *Grimm*, 2002; *Delory et al.*, 2007], time domain electomagnetics [e.g., *Grimm*, 2002; *Grimm et al.*, 2009], or surface nuclear magnetic
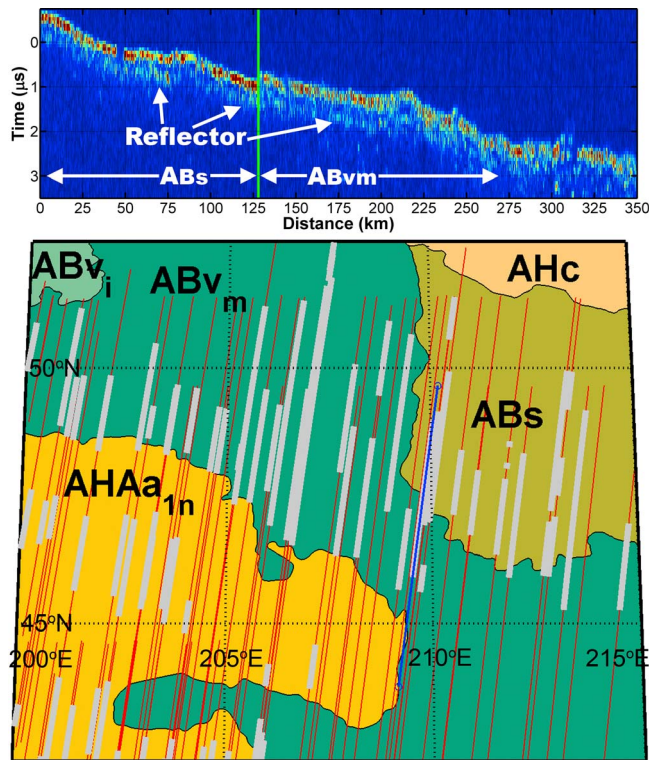
Figure A1. (top) SHARAD track 0390502 showing the reflector that can be found on either side of the Abs/ABv$_m$ boundary (green). (bottom) Map view of the SHARAD track (blue) with reflectors shown in gray and all interpreted tracks shown in red.

resonance [e.g., *Grimm*, 2002, 2003]. Even in areas of low attenuation rates these geophysical techniques are necessary as radar alone cannot uniquely identify groundwater.

[34] A promising use of ground-penetrating radar on Mars is for shallow (meters to tens of meters) investigation to provide subsurface context in support of surface rovers [*Grant et al.*, 2003; *Leuschen et al.*, 2003; *Soldovieri et al.*, 2009]. Ground-based radars can also detect smaller variations in the subsurface as their footprint is much smaller and they have a much higher dynamic range than their orbital counterparts.

Appendix A

[35] We infer that the abundant reflections detected in ABv$_m$ and ABs units (oval in Figure 2) are due to ice-rich material superimposed on the regional geology [*Plaut et al.*, 2009b; *Byrne et al.*, 2009]. These reflectors differ from those in other units in the following ways: reflectors are only detected in these units in this area, all other units that have been altered by water do not have SHARAD reflections, and this is the only region where there are continuous reflectors that cross geologic unit boundaries (Figure A1). *Plaut et al.* [2009b] linked the reflectors in this area with the abundant reflections detected in AAa$_{1n}$ as ice-rich material due to numerous geomorphic indicators. The ABv$_m$ and ABs reflections are shallow (~0.33 μs or ≤25 m at $\varepsilon_1' \geq 4$), while the AAa$_{1n}$ can extend three times as deep. We suggest the

abundant AAa$_{1n}$ reflectors are most likely created by the low losses of a young pristine volcanic unit. However, at latitudes between 43°N and 56°N, direct imaging of ice-rich material has been excavated by very recent impact craters [*Byrne et al.*, 2009]. This excavation occurs over much of the northern hemisphere, but SHARAD reflections are only abundant in this region. We suggest that this ice-rich material may extend slightly deeper, thus allowing it to be detected by SHARAD, and/or there is a geologic layer that acts as a boundary to the ice, thus causing a dielectric contrast in the subsurface.

References

Aki, K., and B. Chouet (1975), Origin of coda waves: Source, attenuation, and scattering effects, *J. Geophys. Res.*, *80*, 3322–3342, doi:10.1029/JB080i023p03322.

Anderson, D. M., and A. R. Tice (1973), The unfrozen interfacial phase in frozen soil water systems, in *Physical Aspects of Soil Water and Salts in Ecosystems*, *Ecol. Stud.*, vol. 4, pp. 107–124, Springer, London.

Annan, A. P. (2003), *Ground Penetrating Radar Principles, Procedures, and Applications*, 286 pp., Sensors and Software, Inc., Mississauga, Ont., Canada.

Asay, D. B., and S. H. Kim (2005), Evolution of the adsorbed water layer structure on silicon oxide at room temperature, *J. Phys. Chem. B*, *109*(35), 16,760–16,763, doi:10.1021/jp053042o.

Beyer, R. A., and A. S. McEwen (2005), Layer stratigraphy of eastern Coprates and northern Capri Chasmata, Mars, *Icarus*, *179*, 1–23, doi:10.1016/j.icarus.2005.06.014.

Bibring, J. P., et al. (2006), Global mineralogical and aqueous Mars history derived from OMEGA/Mars Express data, *Science*, *312*, 400–404, doi:10.1126/science.1122659.

Byrne, S., et al. (2009), Distribution of mid-latitude ground ice on Mars from new impact craters, *Science*, *325*, 1674–1676, doi:10.1126/science.1175307.

Campbell, B., L. Carter, R. Phillips, J. Plaut, N. Putzig, A. Safaeinili, R. Seu, D. Biccari, A. Egan, and R. Orosei (2008), SHARAD radar sounding of the Vastitas Borealis Formation in Amazonis Planitia, *J. Geophys. Res.*, *113*, E12010, doi:10.1029/2008JE003177.

Carrier, W. D., III, G. R. Olhoeft, and W. Mendell (1991), Physical properties of the lunar surface, in *Lunar Sourcebook: A User's Guide to the Moon*, edited by G. H. Heiken, D. T. Vaniman, and B. M. French, pp. 475–594, Cambridge Univ. Press, New York.

Carter, L. M., et al. (2009), Shallow radar (SHARAD) sounding observations of the Medusae Fossae Formation, Mars, *Icarus*, *199*, 295–302, doi:10.1016/j.icarus.2008.10.007.

Clark, R. N. (2009), Detection of adsorbed water and hydroxyl on the Moon, *Science*, *326*, 562–564, doi:10.1126/science.1178105.

Costanzo, P. M. (2001), Baseline studies of the Clay Minerals Society Source Clays: Introduction, *Clays Clay Miner.*, *49*, 372–373, doi:10.1346/CCMN.2001.0490502.

Delory, G. T., et al. (2007), Prospecting for subsurface liquid water using magnetotellurics on Mars, paper 3293 presented at 7th International Conference on Mars, Lunar and Planet. Inst., Pasadena, Calif., 9–13 July.

Fagents, S. A., P. Lanagan, and R. Greeley (2002), Rootless cones on Mars: A consequence of lava-ground ice interaction, *Geol. Soc. Spec. Publ.*, *202*, 295–317, doi:10.1144/GSL.SP.2002.202.01.15.

Feldman, W. C., et al. (2004), Global distribution of near-surface hydrogen on Mars, *J. Geophys. Res.*, *109*, E09006, doi:10.1029/2003JE002160.

Grant, J. A., A. E. Schutz, and B. A. Campbell (2003), Ground penetrating radar as a tool for probing the shallow subsurface of Mars, *J. Geophys. Res.*, *108*(E4), 8024, doi:10.1029/2002JE001856.

Grimm, R. E. (2002), Low-frequency electromagnetic exploration for groundwater on Mars, *J. Geophys. Res.*, *107*(E2), 5006, doi:10.1029/2001JE001504.

Grimm, R. E. (2003), A comparison of time domain electromagnetic and surface nuclear magnetic resonance sounding for subsurface water on Mars, *J. Geophys. Res.*, *108*(E4), 8037, doi:10.1029/2002JE001882.

Grimm, R. E., E. Heggy, S. Clifford, C. Dinwiddie, R. Mcginnis, and D. Farrell (2006), Absorption and scattering in ground penetrating radar:

Analysis of the Bishop Tuff, *J. Geophys. Res.*, *111*, E06S02, doi:10.1029/2005JE002619.

Grimm, R. E., B. Berdanier, R. Warden, J. Harrer, R. Demara, J. Pfeiffer, and R. Blohm (2009), A time-domain electromagnetic sounder for detection and characterization of groundwater on Mars, *Planet. Space Sci.*, *57*, 1268–1281, doi:10.1016/j.pss.2009.05.003.

Gueguen, Y., and V. Palciauckas (1994), *Introduction to the Physics of Rocks*, 392 pp., Princeton Univ. Press, Princeton, N. J.

Holt, J. W., et al. (2008), Radar sounding evidence for buried glaciers in the southern mid-latitudes of Mars, *Science*, *322*, 1235–1238, doi:10.1126/science.1164246.

Jaeger, W. L., L. P. Keszthelyi, A. S. McEwen, C. M. Dundas, and P. S. Russell (2007), Athabasca Valles, Mars: A lava-draped channel system, *Science*, *317*, 1709–1711, doi:10.1126/science.1143315.

Jänchen, J., D. L. Bish, and U. Hellwig (2009), The H$_2$O sorption properties of a Martian dust analog, *Proc. Lunar Planet. Sci. Conf.*, *40th*, 1395.

Johnson, G., G. R. Olhoeft, and R. S. Carmichael (1984), *Handbook of Physical Properties of Rocks*, 360 pp., CRC Press, Boca Raton, Fla.

Kauzmann, W. (1942), Dielectric relaxation as a chemical rate process, *Rev. Mod. Phys.*, *14*, 12–44, doi:10.1103/RevModPhys.14.12.

Keszthelyi, L., W. Jaeger, A. McEwen, L. Tornabene, R. A. Beyer, C. Dundas, and M. Milazzo (2008), High Resolution Imaging Science Experiment (HiRISE) images of volcanic terrains from the first 6 months of the Mars Reconnaissance Orbiter Primary Science Phase, *J. Geophys. Res.*, *113*, E04005, doi:10.1029/2007JE002968.

Lanagan, P. D., A. S. McEwen, L. P. Keszthelyi, and T. Thordarson (2001), Rootless cones on Mars indicating the presence of shallow equatorial ground ice in recent times, *Geophys. Res. Lett.*, *28*, 2365–2368, doi:10.1029/2001GL012932.

Leuschen, C., P. Kanagaratnam, K. Yoshikawa, S. Arcone, and P. Gogineni (2003), Design and field experiments of a ground-penetrating radar for Mars exploration, *J. Geophys. Res.*, *108*(E4), 8034, doi:10.1029/2002JE001876.

Malin, M. C., and K. S. Edgett (2000), Sedimentary rocks of early Mars, *Science*, *290*, 1927–1937, doi:10.1126/science.290.5498.1927.

Malin, M. C., and K. S. Edgett (2003), Evidence for persistent flow and aqueous sedimentation on early Mars, *Science*, *302*, 1931–1934, doi:10.1126/science.1090544.

Mandt, K., S. Silva, J. Zimbelman, and D. Wyrick (2009), Distinct erosional progressions in the Medusae Fossae Formation, Mars, indicate contrasting environmental conditions, *Icarus*, *204*, 471–477, doi:10.1016/j.icarus.2009.06.031.

Matsuoka, T., S. Fujita, and S. Mae (1997), Dielectric properties of ice containing ionic impurities at microwave frequencies, *J. Phys. Chem.*, *101*, 6219–6222, doi:10.1021/jp9631590.

McCafferty, E., and A. C. Zettlemoyer (1971), Adsorption of water vapour on *a*-Fe$_2$O$_3$, *Discuss. Faraday Soc.*, *52*, 239, doi:10.1039/df9715200239.

Michalski, J. R., M. D. Kraft, T. G. Sharp, L. B. Williams, and P. R. Christensen (2006), Emission spectroscopy of clay minerals and evidence for poorly crystalline aluminosilicates on Mars from Thermal Emission Spectrometer data, *J. Geophys. Res.*, *111*, E03004, doi:10.1029/2005JE002438.

Milliken, R. E., J. Mustard, F. Poulet, D. Jouglet, J.-P. Bibring, B. Gondet, and Y. Langevin (2007), Hydration state of the Martian surface as seen by Mars Express OMEGA: 2. H$_2$O content of the surface, *J. Geophys. Res.*, *112*, E08S07, doi:10.1029/2006JE002853.

Nunes, D. C., and R. J. Phillips (2006), Radar subsurface mapping of the polar layered deposits on Mars, *J. Geophys. Res.*, *111*, E06S21, doi:10.1029/2005JE002609.

Olhoeft, G. R. (2003), Subsurface exploration for water on Mars, paper 3213 presented at 6th International Conference on Mars, Lunar and Planet. Inst., Pasadena, Calif., 20–25 July.

Olhoeft, G. R., and D. W. Strangway (1975), Dielectric properties of the first 100 meters of the Moon, *Earth Planet. Sci. Lett.*, *24*, 394–404, doi:10.1016/0012-821X(75)90146-6.

Olhoeft, G. R., D. W. Strangway, and G. W. Pearce (1975), Effects of water on electrical properties of lunar fines, *Proc. Lunar Sci. Conf.*, *6th*, 3333–3342.

Phillips, R. J., et al. (2008), Mars north polar deposits: Stratigraphy, age, and geodynamical response, *Science*, *320*(5880), 1182–1185, doi:10.1126/science.1157546.

Pieters, C. M., et al. (2009), Character and spatial distribution of OH/H$_2$O on the surface of the Moon seen by M3 on Chandrayaan-1, *Science*, *326*, 568–572, doi:10.1126/science.1178658.

Plaut, J. J., et al. (2007), Subsurface radar sounding of the south polar layered deposits of Mars, *Science*, *316*, 92–95, doi:10.1126/science.1139672.

Plaut, J. J., A. Safaeinili, J. W. Holt, R. J. Phillips, J. W. Head III, R. Seu, N. E. Putzig, and A. Frigeri (2009a), Radar evidence for ice in lobate debris aprons in the mid-northern latitudes of Mars, *Geophys. Res. Lett.*, *36*, L02203, doi:10.1029/2008GL036379.

Plaut, J. J., et al. (2009b), A widespread radar-transparent layer detected by SHARAD in Arcadia Planitia, Mars, *Proc. Lunar Planet. Sci. Conf.*, *40th*, 2312.

Putzig, N. E., R. J. Phillips, B. A. Campbell, J. W. Holt, J. J. Plaut, L. M. Carter, A. F. Egan, F. Bernardini, A. Safaeinili, and R. Seu (2009), Subsurface structure of Planum Boreum from Mars Reconnaissance Orbiter Shallow Radar soundings, *Icarus*, *204*, 443–457, doi:10.1016/j.icarus.2009.07.034.

Rieder, R., T. Economou, H. Wänke, A. Turkevich, J. Crisp, J. Brückner, G. Dreibus, and H. Y. McSween Jr. (1997), The chemical composition of Martian soil and rocks returned by the mobile alpha proton X-ray spectrometer: Preliminary results from the X-ray mode, *Science*, *278*, 1771–1774.

Rieder, R., et al. (2004), Chemistry of rocks and soils at Meridiani Planum from the alpha particle X-ray spectrometer, *Science*, *306*, 1746–1749, doi:10.1126/science.1104358.

Rother, H., H. M. Jol, and J. Schulmeister (2007), Stratigraphy and tectonic implicatoins of late Pleistocene valley fill in the Hope Valley, Canterbury, South Island, New Zealand, in *Stratigraphy Analyses Using GPR*, edited by G. S. Baker and H. M. Jol, *Spec. Pap. Geol. Soc. Am.*, *432*, 155–167, doi:10.1130/2007.2432(11).

Schaber, G. G., T. W. Thompson, and S. H. Zisk (1975), Lava flows in Mare Imbrium: An evaluation of anomalously low Earth-based radar reflectivity, *Moon*, *13*, 395–423, doi:10.1007/BF02626384.

Seu, R., D. Biccari, R. Orosei, L. V. Lorenzoni, R. J. Phillips, L. Marinangeli, G. Picardi, A. Masea, and E. Zampolini (2004), SHARAD: The MRO 2005 shallow radar, *Planet. Space Sci.*, *52*, 157–166, doi:10.1016/j.pss.2003.08.024.

Seu, R., et al. (2007a), SHARAD sounding radar on the Mars Reconnaissance Orbiter, *J. Geophys. Res.*, *112*, E05S05, doi:10.1029/2006JE002745.

Seu, R., et al. (2007b), Accumulation and erosion of Mars' south polar layered deposits, *Science*, *317*, 1715–1718, doi:10.1126/science.1144120.

Shahidi, M., J. B. Hasted, and A. K. Jonscher (1975), Electrical properties of dry and humid sand, *Nature*, *258*, 595–597, doi:10.1038/258595a0.

Sjöström, J., J. Swenson, R. Bergman, and S. Kittaka (2008), Investigating hydration dependence of dynamics of confined water: Monolayer, hydration water and Maxwell-Wagner processes, *J. Chem. Phys.*, *128*, 154503, doi:10.1063/1.2902283.

Soldovieri, F., G. Prisco, and S. Hamran (2009), A preparatory study on subsurface exploration on Mars using GPR and microwave tomography, *Planet. Space Sci.*, *57*, 1076–1084, doi:10.1016/j.pss.2008.11.014.

Solomon, S. C., D. L. Anderson, W. B. Banerdt, R. G. Butler, P. M. Davis, F. K. Duennebier, Y. Nakamura, E. A. Okal, and R. J. Phillips (1991), *Scientific Rationale and Requirements for a Global Seismic Network on Mars*, 51 pp., Lunar and Planet. Sci. Inst., Houston, Tex.

Stillman, D. E., R. E. Grimm, and S. F. Dec (2010), Low-frequency electrical properties of soils mixed with saline ice, *J. Phys. Chem. B*, *114*, 6065–6073, doi:10.1021/jp9070778.

Sunshine, J. M., T. L. Farnham, L. M. Feaga, O. Groussin, F. Merlin, R. E. Milliken, and M. F. A'Hearn (2009), Temporal and spatial variability of lunar hydration as observed by the Deep Impact spacecraft, *Science*, *326*, 565–568, doi:10.1126/science.1179788.

Tanaka, K. L., J. A. Skinner, and T. M. Hare (2005), Geologic map of the northern plains of Mars, *U.S. Geol. Surv. Misc. Invest. Ser. Map*, I-2888.

Tittmann, B. R. (1979), Brief note for consideration of active seismic exploration on Mars, *J. Geophys. Res.*, *84*, 7940–7942, doi:10.1029/JB084iB14p07940.

Ulaby, F. T., R. K. Moore, and A. K. Fung (1981), *Microwave Remote Sensing: Active and Passive*, vol. I, *Microwave Remote Sensing Fundamentals and Radiometry*, 456 pp., Addison-Wesley, Reading, Mass.

Vaucher, J., M. J. Baratoux, P. Toplis, P. Pinet, N. Mangold, and K. Kurita (2009), The morphologies of volcanic landforms at Central Elysium Planitia: Evidence for recent and fluid lavas on Mars, *Icarus*, *200*(1), 39–51, doi:10.1016/j.icarus.2008.11.005.

Watters, T. R., et al. (2007), Radar sounding of the Medusae Fossae formation Mars: Equatorial ice or dry, low-density deposits?, *Science*, *318*, 1125–1128, doi:10.1126/science.1148112.

Zimbelman, J. R., and L. J. Griffin (2010), HiRISE images of yardangs and sinuous ridges in the lower member of the Medusae Fossae Formation, Mars, *Icarus*, *205*, 198–210, doi:10.1016/j.icarus.2009.04.003.

R. E. Grimm and D. E. Stillman, Department of Space Studies, Southwest Research Institute, 1050 Walnut St. #300, Boulder, CO 80302, USA. (dstillman@boulder.swri.edu)